Materials Horizons

ROYAL SOCIETY OF CHEMISTRY

COMMUNICATION

View Article Online
View Journal | View Issue

Cite this: *Mater. Horiz.*, 2026, **13**, 464

Received 4th August 2025,
Accepted 2nd October 2025

DOI: 10.1039/d5mh01486g

rsc.li/materials-horizons

Novel ambipolar polymers for detection beyond 1000 nm with organic phototransistors

Kaiyang Wei,[a] Davide Nodari,[a] Xabier Rodríguez-Martínez,[b] Leonidas Tsetseris,[c] Alkmini D. Nega,[de] Antonia Dimitrakopoulou-Strauss,[e] Martina Rimmele,[a] Nikos Hastas,[f] Yijia Li,[a] Flurin Eisner,[g] Manolis Matzapetakis,[d] Jaime Martin,[b] Vasilis G. Gregoriou,[d] Nicola Gasparini,[a] Christos L. Chochos[d] and Julianna Panidi *[ah]

Organic phototransistors (OPTs) hold significant promise for cost-effective, flexible optoelectronic applications, particularly in Short-wave-Infrared (SWIR) detection, which is crucial for applications such as health monitoring, communications, and artificial vision. Traditional OPTs often rely on unipolar materials, limiting their efficiency by utilizing only one type of charge carrier. In contrast, ambipolar organic semiconductors (OSCs), transporting both electrons and holes, can fully harness photogenerated carriers, thereby enhancing device performance. Here, high-performance, solution-processed ambipolar single-component SWIR OPTs are demonstrated by fine-tuning the number of fused thiophene rings in donor–acceptor (D–A) conjugated polymers utilizing thiadiazoloquinoxaline-unit (TQ) as the electron-deficient unit. Through systematic polymer characterizations and optoelectronic device characterizations it was revealed that three fused thiophene rings (TQ-T3) delivered ambipolar NIR phototransistors with well-balanced hole and electron mobilities of 0.03 and 0.02 $cm^2 V^{-1} s^{-1}$ and the highest reported specific detectivity of 2×10^8 Jones (at 1100 nm), with external quantum efficiency of 1400% and 1200% for the p-type and n-type single-component active layer material, respectively. These findings contribute to advancing the design of efficient ambipolar OPTs for SWIR detection, with potential applications in imaging and sensing technologies.

New concepts

Organic semiconductors with high charge carrier ambipolar mobility and light sensitivity in NIR window II are limited and at the same time important for applications in optical quantum information, LiDAR, as well as biometric imaging. Molecular tuning of conjugated polymers allows for the development of materials with targeted properties. Here, we develop new polymers based on a thiadiazoloquinoxaline unit (TQ) and investigate the effect of the addition of fused thiophene rings on the polymer backbone. Interestingly, adding three fused thiophene rings to the TQ-unit, as opposed to two and four, allows for easier alteration of the molecular conformation. This odd–even effect between the TQ-T2, TQ-T3, and TQ-T4 rings is translated into ambipolar charge carrier mobility, with the TQ-T3 outperforming. This enabled us to develop high-performing NIR phototransistors with a response under 1100 nm LED excitation.

1. Introduction

Significant efforts have been made to develop high-sensitivity NIR organic detectors due to the wealth of practical applications in health monitoring,[1] optical communications,[2] and artificial vision[3] in the form of organic photodiodes (OPDs) and phototransistors (OPTs). Although many OPTs have been reported in the literature, NIR detection beyond 1000 nm is less common and, at the same time, is of particular interest because it offers several advantages, such as deeper penetration depth into biological tissues and better image contrast.[4] It also plays a key role in single photon detection for optical quantum information,[5] and LiDAR systems for autonomous vehicles due to accuracy and eye safety standards.[6,7] A current challenge arises from the difficulty of simultaneously achieving a high absorption coefficient in low-bandgap materials and strong NIR absorption.

Utilising ambipolar organic semiconductors with balanced charge transport between holes and electrons and NIR absorption

[a] *Department of Chemistry and Centre for Processable Electronics, Imperial College London, London W12 0BZ, UK*
[b] *Universidade da Coruña, Campus Industrial de Ferrol, CITENI, Campus de Esteiro S/N, 15471 Ferrol, Spain*
[c] *Department of Physics, School of Applied Mathematical and Physical Sciences, National Technical University of Athens, Athens GR-15780, Greece*
[d] *Institute of Chemical Biology, National Hellenic Research Foundation, 48 Vassileos Constantinou Avenue, Athens 11635, Greece*
[e] *Clinical Cooperation Unit Nuclear Medicine, German Cancer Research Center, 69120 Heidelberg, Germany*
[f] *School of Physics, Department of Condensed Matter and Materials Physics, Aristotle University of Thessaloniki, Thessaloniki 54124, Greece*
[g] *School of Materials Science and Engineering, Queen Mary University of London, London, E1 4NS, UK*
[h] *Institute for Integrated Micro and Nano Systems, School of Engineering, University of Edinburgh, Edinburgh, EH8 9YL, UK. E-mail: julianna.panidi@ed.ac.uk*

is of high importance for next-generation integrated circuits.[7–9] For example, ambipolar heterojunction OPTs were able to achieve second-order adaptive metaplasticity and photoadaptation for complex machine vision tasks.[10] In general, most reported OPTs have been based on unipolar semiconductors,[11] which primarily transport one type of charge carrier, either holes (p) or electrons (n), and this is a limitation for circuits and electronics integration. Ambipolar materials allow for the adjustment of charge carrier type by simply reversing the polarity of the applied gate-source and drain-source voltage. The intrinsic ambipolarity of certain organic semiconductors offers a straightforward and versatile approach to switch between n-type and p-type conduction in a single device,[12] thus, enabling a more efficient use of the photogenerated carriers.

Another way to achieve ambipolarity is through thin films of semiconducting polymer blends, and composites produced through solution processing or vacuum co-evaporation. For example, bulk heterojunction (BHJ) electrolyte-gated OPTs were developed from DPP-polymer as donor and $PC_{61}BM$ as the acceptor with a responsivity of 1.5×10^3 A W^{-1}, under 808 nm light illumination.[13] However, precise control over the morphology of these blends is essential for optimising and enhancing ambipolarity.[14] Bilayer configuration, on the other hand, typically comprises sequential deposition of two materials. For example, Lim *et al.*[15] described the development of a novel organic photosensitizer (donor–acceptor-dye donor type small molecule) that significantly enhanced the charge carrier mobility from 0.08 cm^2 V^{-1} s^{-1} to 0.84 cm^2 V^{-1} s^{-1}, and reached a p-type responsivity of 100 A W^{-1} under 850 nm illumination. These improvements were attributed to the photosensitizer layer's ability to enhance exciton dissociation, trap electrons, and increase hole concentration in the channel.

Identifying ambipolar materials to develop high-performing single-component OPTs is important to simplify the manufacturing, lower the cost, and enhance sustainability compared with multicomponent active layers and more complicated device structures. Zhu *et al.*[16] developed NIR-OPTs using single-component D–A conjugated polymer nanowires with a responsivity of 0.44 A W^{-1} for the p-type channel and 0.07 A W^{-1} for the n-type channel under 808 nm. These higher responsivity values than those of thin-film counterparts are attributed to the nanowires' high trap density and large surface-to-volume ratio. Nodari *et al.*[17] reported high-detectivity ambipolar OPTs using heteroatom engineering to enhance performance in NIR detection (peak absorption at ~964 nm). By substituting sulphur with oxygen in the diketopyrrolopyrrole co-polymer, the OPTs demonstrate well-balanced ambipolar behaviour, with responsivities of 69 A W^{-1} and 99 A W^{-1} in the p-type and n-type regimes under 940 nm illumination.

In our search for suitable ambipolar materials with absorption beyond 1000 nm, the thiadiazoloquinoxaline (TQ) containing D–A polymers have emerged as very promising candidates. The TQ unit is a highly electron-deficient moiety. And by combining it with highly electron-rich units, such as thiophene derivatives, the polymer's properties can be fine-tuned. The low bandgap of TQ is attributed to the stabilization of the quinoid form within the polymer's structure, which is known to lower the bandgap by influencing the electron distribution along the backbone.[18] Previous studies[19,20] have shown that a D–A combination consisting of terthiophene and TQ leads to better NIR-II photodetection characteristics than those with one thiophene, due to the enhanced crystallinity imposed by the presence of the increased number of thiophene rings per repeat unit, demonstrating high detectivity NIR OPDs.

Taking this into consideration, we designed the next generation of TQ-based D–A polymers utilizing multifused (2 to 4) thiophene rings as the electron-donating units. A significant advantage of employing fused thiophene rings is that they exhibit a decreased number of possible conformers in a polymer backbone due to "locking" of the torsional rotation *versus* their non-fused thiophene analogues. This can lead to better molecular packing due to their planar, rigid structure, a feature that generally translates to higher mobility in organic thin film transistors.[21,22] Furthermore, the utilization of TQ-based conjugated polymers in OPTs has not yet been explored to the best of our knowledge, and they are of particular interest due to the photocurrent amplification.[23]

Hence, in this work, we tuned the optoelectronic properties of the TQ-containing polymers with fused-ring bonding thiophenes in order to develop single-component organic phototransistors with sensitivity beyond 1000 nm. This was achieved by the synthesis of TQ-based polymers containing two, three, and four fused thiophene rings, namely TQ-T2, TQ-T3, and TQ-T4, respectively, by Stille cross-coupling polycondensation. The TQ-T2 and TQ-T4 demonstrate higher p-type charge transport, with mobilities around 0.015 cm^2 V^{-1} s^{-1} for p-type and 0.004 cm^2 V^{-1} s^{-1} for n-type. However, TQ-T3 exhibits one/two orders of magnitude higher mobilities and more balanced behavior with p-type mobilities of 0.03 cm^2 V^{-1} s^{-1} and n-type of 0.02 cm^2 V^{-1} s^{-1}. We further evaluated their photoresponse under LED illumination at 1100 nm and exhibited well-balanced responsivities of 12 A W^{-1} and 11 A W^{-1}. The external quantum efficiency (EQE) was found to be 1400% and 1200% for the p-type and n-type, respectively. Additionally, a specific detectivity of 2×10^8 Jones was achieved for both p- and n-type OPTs, by measuring the electrical noise of the OPTs. The OPT characteristics are among the highest reported NIR-II OPTs and surpass the values of BHJ devices.[24,25]

2. Results and discussion

2.1 Material synthesis and characterization

The molecular structures of the newly developed TQ-T based polymers are presented in Fig. 1a and Fig. S1, S2. TQ-T2, TQ-T3, and TQ-T4 were synthesized by Stille cross-coupling polymerization (see SI for synthesis), and their resulting weight-average molecular weights are M_w = 83.1, 89.8, and 78.2 kDa, respectively (Fig. S2). The absorption profiles of the TQ-T based polymers are extended in the Shortwave-Infrared (SWIR) range, with absorption onset at 1750 nm, an optical band gap of 0.7 eV, and peak absorption at 1155, 1288 and 1162 nm for the

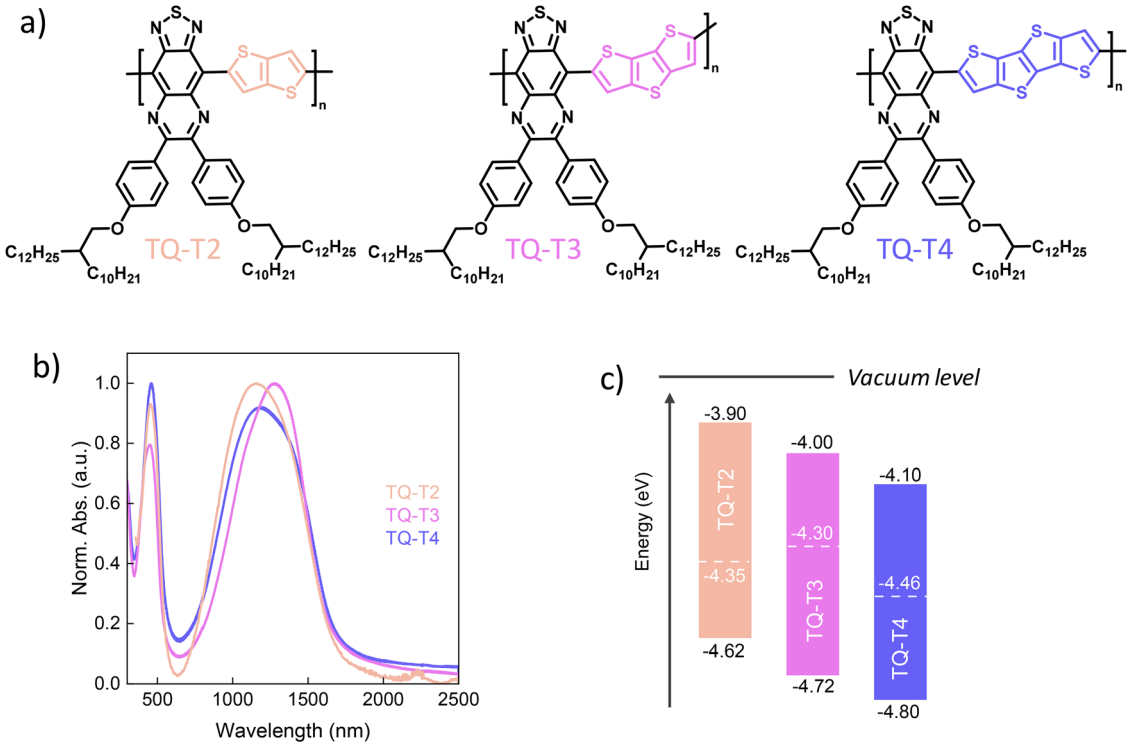

Fig. 1 (a) Molecular structures of the novel polymers based on thiadiazoloquinoxaline-thiophene with two fused rings (TQ-T2), three fused rings (TQ-T3), and four fused rings (TQ-T4). (b) Normalised absorption spectra from thin films, and (c) their corresponding frontier energy levels of materials. The energy of the HOMO is calculated as the inverse of the ionization potential measured by air photoemission spectroscopy (APS) from thin films. LUMO energy levels are estimated by adding the optical band gap to the HOMO level. Fermi levels were obtained by Kelvin probe, and they are marked by dashed lines. (see Fig. S4).

TQ-T2, TQ-T3, and TQ-T4 polymers, respectively as measured from thin films (Fig. 1b). This confirms the molecular design concept to combine a high electron-deficient building block (TQ) with high electron-donating fused thiophene monomers to achieve ultra-small bandgap polymers with tunable properties. We were interested in evaluating the impact of the addition of the fused thiophene rings on the energetics of the polymers from both experimental measurements and theoretical calculations. Upon measuring the ionization potential of the thin films, it was observed that the highest occupied molecular orbitals (HOMO) of the materials were slightly downshifted ($\sim$0.1 eV) *versus* vacuum with the addition of thiophene rings, with TQ-T2 exhibiting a HOMO level of – 4.62 eV, TQ-T3 – 4.72 eV, and TQ-T4 – 4.8 eV. (Fig. 1c) The LUMO levels were calculated from the optical band gap and the measured HOMO level. Oxidation and reduction potentials were further determined using cyclic voltammetry (CV) in electrolyte solution, with ferrocene employed as the internal reference. A summary of the results is provided in the SI (Fig. S5 and Table S1). All three polymers show ambipolar characteristics, however, the reduction of TQ-T3 is much more pronounced compared to TQ-T2 and TQ-T4 (see Fig. S5b), indicating a stronger n-type behaviour.

Density functional theory (DFT) calculations were conducted on periodic polymer chains and polymer fragments, such as monomers, dimers, and trimers. Fig. S6–S8 show the most stable structures of TQ-T2, TQ-T3 and TQ-T4 trimers, along with their respective calculated HOMO and LUMO levels. A slight variation between the measured and calculated energy level values is expected, as it has been observed before.[26] We further exploit the relative orientation of the thiophene groups with respect to the TQ moieties with DFT to gain a better understanding of their molecular configurations. Thus, we considered configurations with the same orientation for all TQ groups (named the parallel TQ sequence) and with an alternating TQ orientation (antiparallel TQ sequence). In the most stable configurations of TQ-T2, TQ-T3, and TQ-T4 trimers, all S atoms in the thiophene groups point towards the quinoxaline units. Hence, this motif is key for the relative stability of each structure (a conclusion which is corroborated also with results on periodic polymer chains) and introduces a noticeable difference between TQ-T3 (with an odd number of thiophene rings) and the other two polymers (TQ-T2 and TQ-T4 with even numbers of thiophene rings). Specifically, the most stable TQ-T3 trimer is of the parallel TQ form, whereas the lowest-energy TQ-T2 and TQ-T4 trimers are of the antiparallel TQ type. Hence, even though the relative stability is also affected by steric constraints and entropic interactions pertaining to the branched side chains (which are here omitted to facilitate the first-principles calculations), the results show an unequivocal relative ease for an alternation between parallel and antiparallel conformations in the TQ-T3 case.

In addition, the DFT results reveal details that are relevant to the carrier transport of the studied polymers. All calculated HOMOs are homogeneously distributed over the whole polymer backbone, but the LUMOs show a slight tendency of localization on the TQ units, which indicates slightly higher p-type charge carrier mobility than n-type. Finally, by calculating the torsion angles between the TQ and the thiophene units, we found that the backbones of the TQ-T2 and TQ-T4 are planar with values close to zero. Instead, TQ-T3 chains show small torsion angles of about 22° and 17°–23° between neighboring thiophene and TQ units, as presented in Fig. S9. A summary of the measured and calculated energy levels is presented in Table S2, showcasing a slightly deeper HOMO/LUMO for the TQ-T3 compared with the TQ-T2 and TQ-T4 from the DFT and CV measurements.

2.2 Thin film microstructural analysis

To gain an insight into the film microstructure, grazing incidence wide-angle X-ray scattering (GIWAXS) experiments performed on the TQ-T series of polymers are shown in Fig. 2a, c and e, with the corresponding integrated linecuts in the out-of-plane (OOP) and in-plane (IP) directions shown in Fig. 2b, d and f. All diffractograms share a common pattern consisting of a lamellar peak better resolved in the IP direction (q_{100} = 1.90–1.97 nm^{-1}) and a π–π stacking peak in the OOP direction ($q_{\pi-\pi}$ = 16.97–17.91 nm^{-1}), which indicates the existence of primarily face-on oriented crystallites in the studied polymer films. All polymers appear to be fairly amorphous, with TQ-T3 showing closer lamellar packing (3.18 nm) than TQ-T2 (3.31 nm) and TQ-T4 (3.31 nm). On the other hand, the π–π stacking spacing is slightly larger for the TQ-T3 (0.37 nm) than TQ-T2 and TQ-T4 (0.35 nm). A third broad peak common to all polymers and integrated linecuts is located at q = 13.71–13.97 nm^{-1}. Such a peak shows a weak, isotropic (ring-like) intensity distribution in the corresponding 2D GIWAXS diffractograms and is hypothesized to correspond to the amorphous packing of the branched side-chains in the TQ-T2-4 series. A more detailed analysis of their microstructure revealed that the X-ray crystalline coherence length (CCL) of TQ-T3 is significantly decreased to 6.6 nm compared to the TQ-T2 and TQ-T4 which was found at around 14 nm for both (Table S3).

2.3. Ambipolar organic thin film transistors

OTFTs were fabricated from TQ-T2, TQ-T3, and TQ-T4 polymers in bottom-contact, top-gate (BC-TG) configuration on self-assembled monolayer (SAM) modified gold electrodes, with PMMA as the dielectric layer and aluminium as the gate electrode. Their representative output curves are presented in Fig. S9. While all three polymers demonstrate ambipolar transport, TQ-T2 and TQ-T4 exhibit more p-type, and TQ-T3 shows well-balanced transfer characteristics. TQ-T2 exhibits a p-type mobility of 0.015 cm^2 V^{-1} s^{-1}, with minimal threshold voltage shift as the drain voltage increases, while its n-type mobility is significantly lower at 0.001 cm^2 V^{-1} s^{-1}, accompanied by a threshold voltage shift to a higher value of 38 V. TQ-T4 shows similar behaviour to TQ-T2 and displays a lower off-state current, with p- and n-type mobilities of 0.009 and 0.002 cm^2 V^{-1} s^{-1}, respectively. The p-type threshold voltage of TQ-T4 is −0.5 V, which is lower than that of TQ-T2 (−4.4 V). On the other hand, TQ-T3-based OTFTs exhibit both p-type and n-type

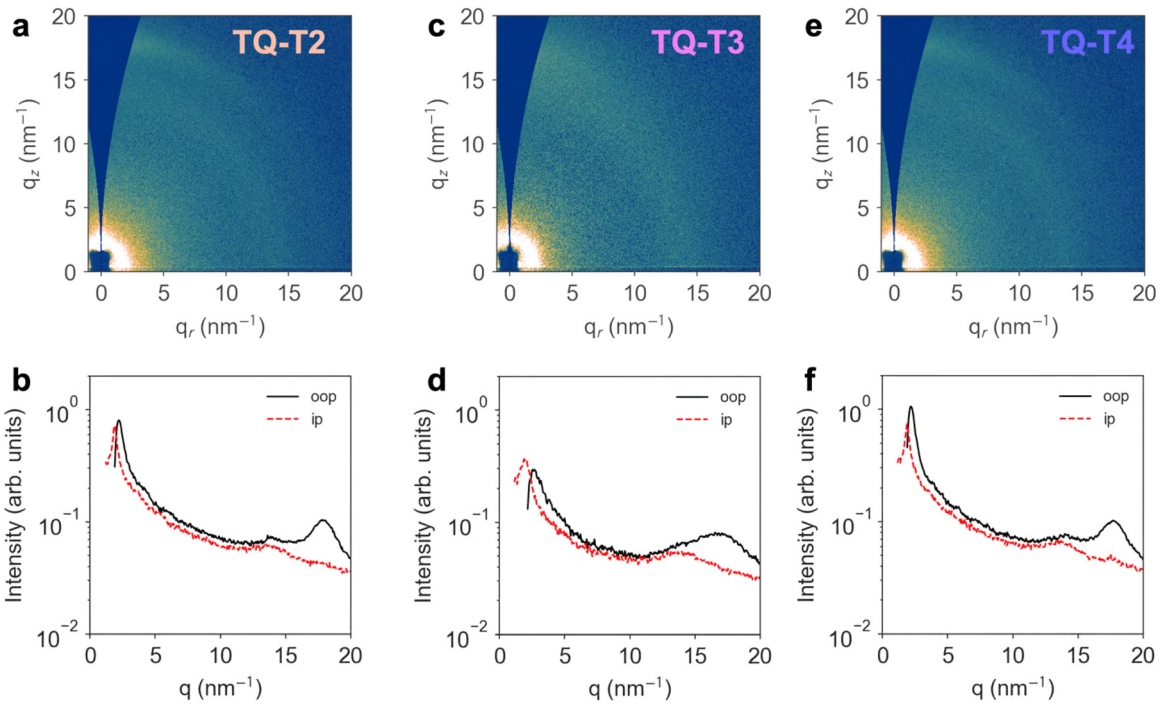

Fig. 2 2D GIWAXS patterns and the corresponding integrated out-of-plane (oop) and in-plane (ip) linecuts of the polymers TQ-T2 (a) and (b); TQ-T3 (c) and (d); and TQ-T4 (e) and (f).

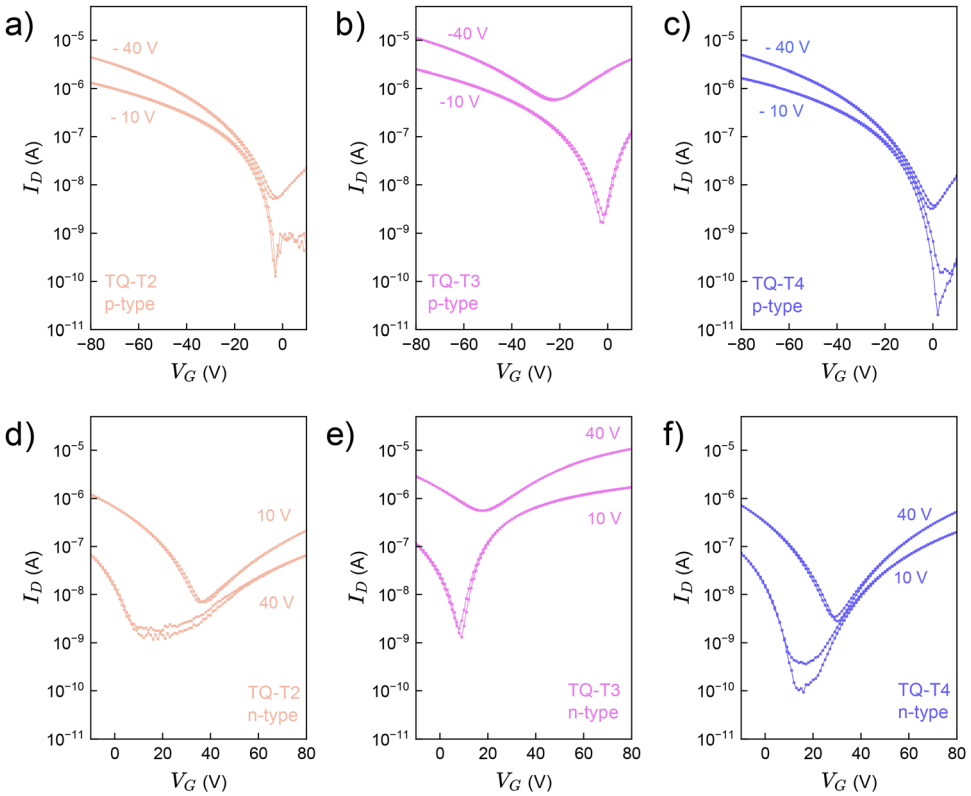

Fig. 3 Representative transfer curves of organic thin film transistors from (a) and (d) TQ-T2, (b) and (e) TQ-T3, and (c) and (f) TQ-T4 OPTs under p-type and n-type operation at V_D = ±10 and 40 V. OTFTs with channel length of 30 μm and width of 1000 μm.

threshold voltages closer to 0 V, with corresponding carrier mobilities of 0.03 $cm^2\ V^{-1}\ s^{-1}$ and 0.02 $cm^2\ V^{-1}\ s^{-1}$, respectively. As a result, TQ-T3 OTFTs demonstrate the highest and most balanced p-type and n-type source-drain currents associated with very small threshold voltages as seen in Fig. 3b, e and Table S4. The latter indicates a good energetic alignment between TQ-T3 and the device contacts, as well as a low trap concentration leading to higher charge carrier transport. It's worth noting that we did not investigate further the charge carrier transport of the materials in single-component devices (p or n-type operation), as our focus was on ambipolar OTFTs.

In order to further demonstrate the potential of the TQ-T3 based OTFTs, we developed complementary-like voltage inverters, the building blocks logic architectures, by integrating two OTFTs operating in the first and third quadrants.[27] This unique operation[28] is based on the ambipolarity of organic semiconductors and, in this case, the TQ-T3. Fig. S10 demonstrates the voltage transfer characteristics along with the calculated signal gain of around 8 operated at V_{dd} = ±70 V. The calculated noise margin low was found at around 49.1% for the p-type and 57.1% for the n-type from the ideal $V_{dd}/2$ value.

In addition, the extended absorption of TQ-T3 in the SWIR window allowed us to develop organic phototransistors. A 1100 nm LED with power intensity (P_{in}) ranging from 1.3 × 10^{-4} to 8.2 × 10^{-2} W cm^2 was used for OPT characterizations, with converted brightness levels of 0.1% and 100% brightness (power increments in Table S5, SI). OPTs generate charge carriers when exposed to light, working alongside the conventional gate control to modulate transistor operation, and function either through a photovoltaic effect (in accumulation mode) or photoconductive effect (in depletion mode).[29] Fig. 4a and b show the characteristic transfer characteristics variation upon increasing light intensities when drain voltages V_D are ±10 V. A clear enhancement in the source-to-drain current is observed as the light intensity increases, and the threshold voltage and charge carrier mobility variation upon light are shown in Fig. S11. The excellent OPT behaviour of the TQ-T3 is also highlighted by the very small threshold voltages *i.e.*, for p-type, V_{th} is close to zero, whereas for n-type is around 9–10 V. The increase in the mobility and the positive shift of V_{th} with higher light power intensity are aligned with the rise of the drain current upon illumination. This indicates that traps are filled not only by the applied positive voltage but also by charges generated through light absorption (photogenerated charges).[30] When a positive voltage is applied, the separated holes from photo-induced excitons are likely to recombine with electrons, which limits n-type transport and causes a positive shift in the threshold voltage. Considering the ultra-narrow bandgap of TQ-T3, it can be inferred that the recombination rate is high. To further evaluate the OPT performance, we calculated the responsivity (R) for p and n-type operation, of which dependence on the V_G and V_D is displayed in Fig. 4c and d. R shows well-balanced values of 12 A W^{-1} for p-type and 11 A W^{-1} for n-type when light intensity is at the lowest (1.36 × 10^{-4} W cm^{-2}), while photosensitivity P

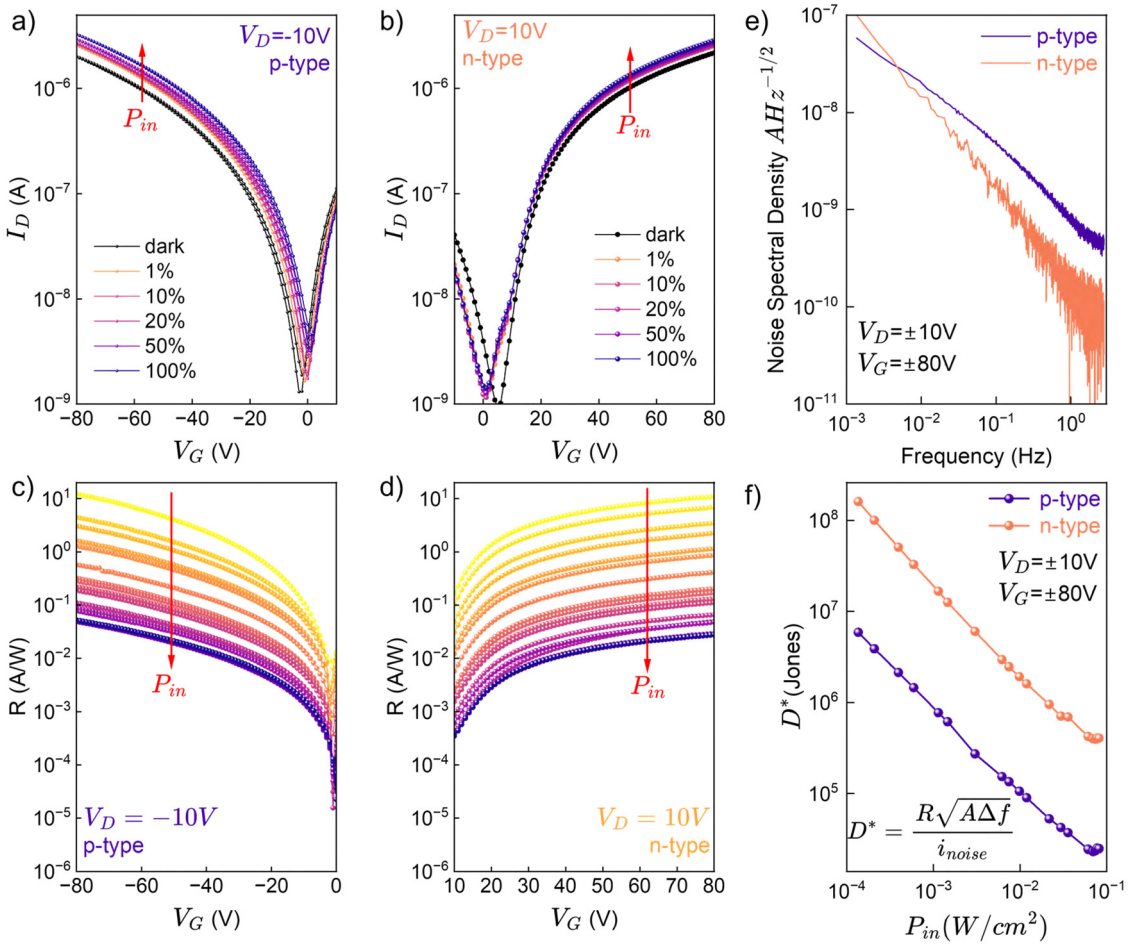

Fig. 4 TQ-T3 OPTs Characterisation: Transfer characteristics upon varying light intensity (Table S5) using a 1100 nm LED for (a) p-type TQ-T3, and (b) n-type TQ-T3. (c) Calculated responsivity (R) with varying $B = V_G$ and light intensity for (c) p-type, and (d) n-type OPTs. (e) The noise spectral density as measured for both p- and n-type operation under V_G = ±80 V and V_D = ±10 V and (f) specific detectivity *vs.* light intensity.

(Fig. S12) displays values of 0.63 and 0.3, for p and n-type, respectively, when light intensity is at the maximum (8.18 × 10^{-2} W cm^{-2}). The external quantum efficiency (EQE) was also calculated, based on EQE = $R \times E_{ph}/e$, where R is the responsivity, E_{ph} the standard photon energy and e the elemental charge. For the p-type OPTs EQE was found to be 1400% and 1200% for the p-type and n-type.[17]

Finally, an important characteristic of photodetectors is the specific detectivity D^* which is a measure of R and the electronic noise spectral density of the device, normalized by the area of the photodetector to enable comparability between different photodetectors.[17] The variation of D^* upon varying the light intensity at a fixed V_G and V_D is presented in Fig. 4f upon measuring the noise *via* dark current recorded with a Keithley 4200, followed by a fast Fourier transform. The noise spectral density is presented in Fig. 4e. D^* values of 6 × 10^6 and 2 × 10^8 Jones, which are the highest ever reported for ambipolar single-component OPTs under 1100 nm excitation, are achieved for p- and n-type OPTs, respectively (see Table S6 for comparison with ambipolar OPTs in the literature). The D^* vs frequency is presented in Fig. S12d. To compare with values reported in literature, D^* using calculated noise are 2.6 × 10^9 and 2.3 × 10^9 Jones for p- and n-type, respectively, with noise level around 8 × 10^{-13} A $Hz^{-1/2}$. This result aligns with theoretical expectations, which suggests that calculating the noise leads to an underestimation of the electronic noise level of the devices (*i.e.* an overestimation of D^*). Finally, the temporal response of the OPTs is presented in Fig. S13 is in the order of hundreds ms, similarly to reported values in the literature.[17,31,32] We believe that with further device engineering approaches, the response speed can be increased. Parameters such as the dielectric capacitance, charge carrier mobility and channel's dimensions all play a crucial role in the response speed.

3. Conclusion

This study successfully demonstrates the development and characterization of high-performance ambipolar OPTs specifically tailored for SWIR detection. This was achieved by careful molecular design of the different fused thiophene rings in

multifused thiophene-based D–A conjugated polymers with TQ as the A unit. Results based on DFT calculations suggest that the superior performance of TQ-T3 may arise from the ability to easily alternate between parallel and antiparallel conformation in its lowest energy. TQ-T3 exhibited well-balanced ambipolar transport with hole and electron mobilities of 0.03 $cm^2 V^{-1} s^{-1}$ and 0.02 $cm^2 V^{-1} s^{-1}$, respectively, that allowed us to develop CMOS-like inverters from two identical devices. Upon exciting the OPTs with a 1100 nm LED light, a maximum responsivity of 12 A W^{-1} in p-type operation and 11 A W^{-1} in n-type was observed with specific detectivities (D^*) reaching up to 2×10^8 Jones in the n-type mode by measuring the noise of the devices and 2×10^9 Jones for both transport types by calculating noise. These results reveal an odd–even thiophene effect, where odd-numbered thiophene rings (TQ–T3) show conformational advantages over even-numbered rings (2 and 4), providing a new design consideration that may guide future molecular engineering strategies new SWIR OSCs with enhanced ambipolar transport characteristics that will boost the performance in OPTs and will be capable of highly sensitive and specific SWIR detection applications.

4. Experimental section

4.1. Grazing incidence wide-angle X-ray scattering (GIWAXS)

GIWAXS experiments were performed at NCD-SWEET beamline at NCD-SWEET beamline at ALBA Synchrotron using an X-ray beam of 12.4 keV at an angle of incidence of 0.12°. Samples were illuminated for 1 s (in air) to avoid degradation. Scattering patterns were acquired using a Rayonix LX255-HS detector, which was positioned at 203.45 mm away from the samples. Polymer films were prepared on Silicon substrates from solutions of 15 mg ml^{-1} in tetralin. Films were spin-coated at 2000 rpm for 30 seconds followed by followed by 100 °C annealing for 10 minutes.

For data analysis, the diffractogram of a bare silicon substrate was collected at the selected angle of incidence (0.12°) and 70% of its intensity used as baseline. Such a baseline (background) was subtracted to the raw GIWAXS diffractograms before performing the azimuthal integrations using pyFAI. Diffraction peaks were fitted[33] according to Pseudo-Voigt functions while using an exponential decay and a linear function as background.

The crystalline coherence length (CCL) was determined based on Scherrer's equation (eqn (1)) to determine the crystallite size:

$$\mathrm{CCL} = 2\pi K/\Delta q, \quad (1)$$

where K is the shape factor (0.9) and Δq is the full width at half maximum of the diffraction peak. The paracrystalline disorder parameter (g) was calculated from eqn (2):

$$g = \sqrt{\frac{\Delta q}{2\pi q_0}}, \quad (2)$$

where q_0 is the peak centre position (scattering vector).

4.2. Air photoemission spectroscopy (APS)

Polymers were deposited on a conductive ITO substrate. The HOMO energy level and their work function were measured by a KP Technology SKP5050/APS02 set-up, with silver as the reference sample. Films were prepared as discussed in GIWAXS section.

Cyclovoltammetry (CV) experiments were performed with a Metrohm Autolab PGSTAT101 Electrochemical analyser and spectra collected on NOVA software. The experiment was set up using a Ag/Ag^+ reference electrode and a Pt wire counter electrode. The polymers were drop-casted on the glassy carbon working electrode and measurements taken at a scan rate of 0.1 V s^{-1} with tetrabutylammonium hexafluorophosphate in acetonitrile (0.1 M) as the supporting electrolyte.

4.3. DFT calculations

The results on monomers, dimers and trimers were obtained with the NWChem code[34] the hybrid B3LYP[35,36] exchange–correlation (xc) functional and the DZVP DFT Orbital basis.[37] Structures were rendered with the software VESTA.[38] The results on the polymer periodic chains were obtained with the DFT code VASP,[39] the PBE xc-functional,[40] projector augmented waves,[41] and an energy cut-off of 500 eV for the plane wave orbital basis. The van der Waals interactions were included with the so-called DFT-D3 method.[42]

4.4. OTFTs fabrication

Bottom-contact, top-gate field-effect transistors were fabricated on glass substrates using TQ-T2, TQ-T3 and TQ-T4 polymers in 15 mg ml^{-1} solutions from tetralin. Glass substrates were sonicated in a Decon 90 water solution, followed by sequential sonication in acetone and isopropanol. 40 nm of Au were thermally evaporated through shadow masks to pattern the source and drain electrodes with channel lengths varying from 30–100 μm and width of 1000 μm. Au electrodes were treated with UV-ozone for 30 min. Au was then immersed for 10 min in 5 mM pentafluorobenzenethiophenol (PFBT) in an isopropanol solution before the active layer deposition for modification. Prior the deposition, polymer solutions were heated at 60 °C for 1 hour. The active layer was spin coated at 2000 rpm for 30 seconds, followed by 100 °C annealing for 10 minutes. 80 mg ml^{-1} PMMA was dissolved in butyl acetate and deposited by spin coating at 2000 rpm for 60 seconds to produce a 560 nm thick dielectric layer, with C_i = 5 nF cm^{-2}. The PMMA gate dielectric was annealed at 80 °C for 30 minutes. Finally, 50 nm of thermally evaporated Aluminium was deposited through a shadow mask for the gate electrode. Device fabrication and optoelectronic characterization were conducted in a nitrogen-filled glovebox with a Keithley 4200 parameter analyser. The same devices that were characterised as OTFTs were used as OPTs. For the OPT characterisation we used a 1100 nm LED from Thorlabs to illuminate the device. The light intensity of the LED was calibrated by a Silicon diode S122C from Thorlabs. To evaluate the temporal response of the OPTs to an external light signal, OPTs were illuminated with a 1100 nm LED of

8.18×10^{-2} W cm^{-2} with a 1 Hz squared-pulsed wave with V_G = ±20 V and V_D = ±10 V. The noise spectral density was extracted from the dark current density, as measured wit the Keithley 4200 parameter analyser with V_D = ±10 V and different V_G, followed by a fast Fourier transform. All the formulas for the characterization of OTFTs and OPTs were based on our previous work.[17]

The external quantum efficiency (EQE) of the phototransistor was estimated from:[43]

$$\mathrm{EQE} = \frac{Rhc}{q\lambda}100\%.$$

Conflicts of interest

The authors declare no conflicts of interest.

Data availability

The data supporting this article have been included as part of the supplementary information (SI). Supplementary information is available. See DOI: https://doi.org/10.1039/d5mh01486g.

Raw data are available upon request from the authors.

Acknowledgements

GIWAXS experiments were performed at NCD-SWEET beamline at ALBA Synchrotron (experiment ID AV-2024028192) with the collaboration of ALBA staff. C.L.C., V.G.G., A.D.-S. and A.N. would like to thank the Helmholtz European partnering program for the cooperation between German Cancer Research Center (DKFZ) and National Hellenic Research Foundation (NHRF) to build the Athens Comprehensive Cancer Center (ACCC) for the financial support. Moreover, the research project was supported by the Hellenic Foundation for Research and Innovation (H.F.R.I.) under the "2nd Call for H.F.R.I. Research Projects to Support Faculty Members & Researchers" (Project Number: 4697). The DFT calculations used the GRNET ARIS HPC resources under project 17011. The authors would like to thank funding from EPSRC council EPSRC; EP/V057839/1.

References

1 H. Xu, J. Li, B. H. K. Leung, C. C. Y. Poon, B. S. Ong, Y. Zhang and N. Zhao, *Nanoscale*, 2013, **5**, 11850.
2 H. Han, Y. J. Lee, J. Kyhm, J. S. Jeong, J. H. Han, M. K. Yang, K. M. Lee, Y. Choi, T. H. Yoon, H. Ju, S. Kyun Ahn and J. A. Lim, *Adv. Funct. Mater.*, 2020, **30**, 2006236.
3 X. Huang, Y. Liu, G. Liu, K. Liu, X. Wei, M. Zhu, W. Wen, Z. Zhao, Y. Guo, Y. Liu, X. Huang, Y. Liu, G. Liu, K. Liu, X. Wei, M. Zhu, W. Wen, Z. Zhao and Y. Guo, *Adv. Funct. Mater.*, 2023, **33**, 2208836.
4 E. Hemmer, A. Benayas, F. Légaré and F. Vetrone, *Nanoscale Horiz.*, 2016, **1**, 168.
5 R. H. Hadfield, *Nat. Photonics*, 2009, **3**(12), 696.
6 M. Dummer, K. Johnson, S. Rothwell, K. Tatah and M. K. Hibbs-Brenner, Proceedings Volume 11692, Optical Interconnects XXI; 116920C, 2021, DOI: 10.1117/12.2577885.
7 E. C. P. Smits, T. D. Anthopoulos, S. Setayesh, E. Van Veenendaal, R. Coehoorn, P. W. M. Blom, B. De Boer and D. M. De Leeuw, *Phys. Rev. B: Condens. Matter Mater. Phys.*, 2006, **73**, 205316.
8 U. Jeong, G. Tarsoly, J. Lee, Y. Eun, J. Do and S. Pyo, *Adv. Electron. Mater.*, 2019, **5**, 1800652.
9 Y. Zhang, Y. Wang, C. Gao, Z. Ni, X. Zhang, W. Hu and H. Dong, *Chem. Soc. Rev.*, 2023, **52**, 1331.
10 Y. Wang, S. Nie, S. Liu, Y. Hu, J. Fu, J. Ming, J. Liu, Y. Li, X. He, L. Wang, W. Li, M. Yi, H. Ling, L. Xie and W. Huang, *Adv. Mater.*, 2024, **36**, 2404160.
11 Y. S. Guan, J. Qiao, Y. Liang, H. K. Bisoyi, C. Wang, W. Xu, D. Zhu and Q. Li, *Light: Sci. Appl.*, 2022, **11**, 1.
12 Y. Zhang, Y. Wang, C. Gao, Z. Ni, X. Zhang, W. Hu and H. Dong, *Chem. Soc. Rev.*, 2023, **52**, 1331.
13 H. Xu, Q. Zhu, Y. Lv, K. Deng, Y. Deng, Q. Li, S. Qi, W. Chen and H. Zhang, *ACS Appl. Mater. Interfaces*, 2017, **9**, 18134.
14 S. Park, B. Lee, B. Bae, J. Chai, S. Lee and C. Kim, *Synth. Met.*, 2019, **253**, 40.
15 D. H. Lim, D. H. Lim, M. Kang, S. Y. Jang, K. Hwang, I. B. Kim, E. Jung, Y. R. Jo, Y. J. Kim, J. Kim, H. Choi, T. W. Kim, S. Mathur, B. J. Kim and D. Y. Kim, *ACS Appl. Mater. Interfaces*, 2020, **12**, 25066.
16 M. Zhu, S. Lv, Q. Wang, G. Zhang, H. Lu and L. Qiu, *Nanoscale*, 2016, **8**, 7738.
17 D. Nodari, S. Sharma, W. Jia, A. V. Marsh, Y. H. Lin, Y. Fu, X. Lu, A. Russkikh, G. T. Harrison, S. Fatayer, N. Gasparini, M. Heeney and J. Panidi, *Adv. Mater.*, 2024, **36**, 2402568.
18 Z. Chen, X. Wei, J. Huang, Y. Zhou, W. Zhang, Y. Pan and G. Yu, *ACS Appl. Mater. Interfaces*, 2019, **11**, 34171.
19 P. Jacoutot, A. D. Scaccabarozzi, T. Zhang, Z. Qiao, F. Aniés, M. Neophytou, H. Bristow, R. Kumar, M. Moser, A. D. Nega, A. Schiza, A. Dimitrakopoulou-Strauss, V. G. Gregoriou, T. D. Anthopoulos, M. Heeney, I. McCulloch, A. A. Bakulin, C. L. Chochos and N. Gasparini, *Small*, 2022, **18**, 2200580.
20 P. Jacoutot, A. D. Scaccabarozzi, D. Nodari, J. Panidi, Z. Qiao, A. Schiza, A. D. Nega, A. Dimitrakopoulou-Strauss, V. G. Gregoriou, M. Heeney, C. L. Chochos, A. A. Bakulin and N. Gasparini, *Sci. Adv.*, 2023, **9**, eadh2694.
21 W. Zhuang, S. Wang, Q. Tao, W. Ma, M. Berggren, S. Fabiano, W. Zhu and E. Wang, *Macromolecules*, 2021, **54**, 970.
22 S. Attar, R. Yang, Z. Chen, X. Ji, M. Comí, S. Banerjee, L. Fang, Y. Liu and M. Al-Hashimi, *Chem. Sci.*, 2022, **13**, 12034.
23 P. C. Y. Chow, N. Matsuhisa, P. Zalar, M. Koizumi, T. Yokota and T. Someya, *Nat. Commun.*, 2018, **9**, 4546.
24 H. Han, S. Nam, J. Seo, C. Lee, H. Kim, D. D. C. Bradley, C. S. Ha and Y. Kim, *Sci. Rep.*, 2015, **5**, 1.
25 X. Yu, H. Lin, Z. He, X. Du, Z. Chen, G. Yang, C. Zheng and S. Tao, *ACS Appl. Mater. Interfaces*, 2023, **15**, 16918.
26 J. Bertrandie, J. Han, C. S. P. De Castro, E. Yengel, J. Gorenflot, T. Anthopoulos, F. Laquai, A. Sharma, D. Baran,

J. Bertrandie, J. Han, C. S. P. De Castro, E. Yengel, J. Gorenflot, T. Anthopoulos, F. Laquai, A. Sharma and D. Baran, *Adv. Mater.*, 2022, **34**, 2202575.
27 W. J. Zeng, X. Y. Zhou, X. J. Pan, C. L. Song and H. L. Zhang, *AIP Adv.*, 2013, **3**, 12101.
28 T. D. Anthopoulos, S. Setayesh, E. Smits, M. Cölle, E. Cantatore, B. De Boer, P. W. M. Blom and D. M. De Leeuw, *Adv. Mater.*, 2006, **18**, 1900.
29 Y. C. Lin, W. C. Yang, Y. C. Chiang and W. C. Chen, *Small Sci.*, 2022, **2**, 2100109.
30 G. Wang, K. Huang, Z. Liu, Y. Du, X. Wang, H. Lu, G. Zhang and L. Qiu, *ACS Appl. Mater. Interfaces*, 2018, **10**, 36177.
31 Q. He, A. Basu, H. Cha, M. Daboczi, J. Panidi, L. Tan, X. Hu, C. C. Huang, B. Ding, A. J. P. White, J. Kim, J. R. Durrant, T. D. Anthopoulos and M. Heeney, *Adv. Mater.*, 2023, **35**, 2209800.
32 Z. Bahrami, K. Schnittker, W. Adi, A. Beisenova, F. Yesilkoy, D. Thompson and J. Andrews, *Adv. Opt. Mater.*, 2024, **12**, 2401269.
33 M. Wojdyr, *J. Appl. Crystallogr.*, 2010, **43**, 1126.
34 M. Valiev, E. J. Bylaska, N. Govind, K. Kowalski, T. P. Straatsma, H. J. J. Van Dam, D. Wang, J. Nieplocha, E. Apra, T. L. Windus and W. A. De Jong, *Comput. Phys. Commun.*, 2010, **181**, 1477.
35 P. J. Stephens, F. J. Devlin, C. F. Chabalowski and M. J. Frisch, *J. Phys. Chem.*, 1994, **98**, 11623.
36 A. D. Becke, *J. Chem. Phys.*, 1993, **98**, 5648.
37 N. Godbout, D. R. Salahub, J. Andzelm and E. Wimmer, *Can. J. Chem.*, 1992, **70**, 560.
38 K. Momma and F. Izumi, *J. Appl. Crystallogr.*, 2011, **44**, 1272.
39 G. Kresse and J. Furthmüller, *Phys. Rev. B: Condens. Matter Mater. Phys.*, 1996, **54**, 11169.
40 J. P. Perdew, K. Burke and M. Ernzerhof, *Phys. Rev. Lett.*, 1996, **77**, 3865.
41 P. E. Blöchl, *Phys. Rev. B: Condens. Matter Mater. Phys.*, 1994, **50**, 17953.
42 S. Grimme, J. Antony, S. Ehrlich and H. Krieg, *J. Chem. Phys.*, 2010, **132**, 154104.
43 Y. Li, M. Pan, Z. Wang, R. Wu, C. Zhang and C. Liu, *Phys. Status Solidi RRL*, 2021, **15**, 2100316.

